Conference on Modelling Fluid Flow (CMFF'22)
The 18th International Conference on Fluid Flow Technologies
Budapest, Hungary, August 30 -September 2, 2022

STUDY OF THE INFLUENCE OF THERMODYNAMIC EFFECTS ON VENTURI CAVITATION FLOW

Xu MENG[1], Le XIANG[2], Kaifu XU[3], Bo LI[4], Huan HAN[5], Shuhong LIU[6], Zhigang ZUO[7]

[1] State Key Laboratory of Hydro Science and Engineering, and Department of Energy and Power Engineering, Tsinghua University. Beijing 100084, China. E-mail: zgbh.mx@163.com
[2] Xi'an Aerospace Propulsion Institute, Xi'an 710100, Shaanxi, China.
[3] Xi'an Aerospace Propulsion Institute, Xi'an 710100, Shaanxi, China.
[4] State Key Laboratory of Hydro Science and Engineering, and Department of Energy and Power Engineering, Tsinghua University, Beijing 100084, China.
[5] College of Robotics, Beijing Union University, Beijing 100020, China
[6] Corresponding Author. State Key Laboratory of Hydro Science and Engineering, and Department of Energy and Power Engineering, Tsinghua University, Beijing 100084, China. E-mail: liushuhong@mail.tsinghua.edu.cn
[7] Corresponding Author. State Key Laboratory of Hydro Science and Engineering, and Department of Energy and Power Engineering, Tsinghua University, Beijing 100084, China. E-mail: zhigang200@mail.tsinghua.edu.cn

ABSTRACT

Research on cavitation flow in thermosensitive conditions is important since the thermodynamic effects are too strong to ignore. Due to the limitation of the measurement technology, and the difficulties of experiments, experimental dynamic results and field results are few. Numerical simulation research is needed to provide more results of thermosensitive conditions and more information on the flow field.

This paper focuses on both the experimental and numerical study of the cavitation flows in a specific Venturi structure with particular emphasis on the dynamic evolution and the thermodynamic effects. A blow-down type water tunnel is built to conduct experiments with water in a wide range of water temperatures and the high-speed photography of the upper side avoids the misjudgement of cavitation break-off caused by the cavity superposition spanwise. For comparison, working conditions same as the experiments are numerically investigated. Good agreements are obtained between the experimental measurements and the numerical results, including the area of cavitation and its frequency. A corrected ZGB cavitation method is used and different turbulence models are compared. k-ε model better simulates the cavitation structure in this research. Results also show that the mean cavitation length/cavitation area decreases when the kappa number increases and the thermodynamic effects parameter increases, which means the thermodynamic effects suppress the cavitation flow and the cavitation-related pressure recovery is reduced. Also, the cavitation is more stable and the collapse and rebound processes of cavity clouds and clusters at the Venturi throat are less violent in larger Σ. Stronger thermodynamic effects are observed at a higher temperature.

Keywords: Cavitation flow; Thermodynamic effects; Venturi

NOMENCLATURE

c_p	[J/(g·K)]	isobaric heat capacity
f	[Hz]	frequency
f_v	[-]	mass fraction
H	[m]	height
L	[kJ/kg]	latent heat
L_{cav}	[m]	length of cavity cloud
P	[Pa]	pressure
P_a	[Pa]	atmosphere
T	[K]	temperature
u	[m/s]	velocity
vf	[m/s]	volume fraction
α_l	[cm^2/s]	liquid thermal diffusivity
κ	[-]	pressure recovery coefficient
λ	[W/(m·K)]	thermal conductivity
ν_l	[m^2/s]	kinematic viscosity
ρ	[kg/m^3]	density
Σ	[-]	thermodynamic parameter
σ	[-]	cavitation number

Subscripts and Superscripts

l	liquid phase
v	vapour phase
in	at the inlet of the Venturi
out	at the outlet of the Venturi
th	at the throat of the Venturi
∞	free-stream
m	mixture

1. INTRODUCTION

A large number of research studies have focused on the cavitation flows in fluid machinery such as turbines and pumps [1,2]. Cavitation flow is formed by the rapid pressure change in the working liquid, which will lead to the formation of small cavities in places where the local pressure is lower than the saturated vapor pressure. Its occurrence sometimes brings negative impacts such as structural vibration, pressure fluctuations, and performance deterioration. Phase change and heat transfer exist when cavitation occurs, which reduces the temperature at the bubble wall and generates a thermal boundary layer around the bubble. The decrease in temperature reduces the saturated vapor pressure of the surrounding liquid, thereby affecting the subsequent growth and collapse of cavitation bubbles and changing the cavitation flow. This process describes the thermodynamic effects of cavitating flow [3,4].

In some special scenes, cryogenic liquids are used as working liquids work and work under thermosensitive conditions. For example, liquid hydrogen and liquid oxygen are fuels of some liquid rockets. When fuels flow through the inducer of the turbine in a liquid rocket engine, cavitation is inevitable. Cavitation may also occur in LNG transportation. The thermodynamic effects are too strong to be ignored for fluids working under thermosensitive conditions [5]. Therefore, the thermodynamic effects of cavitation must be considered in cryogenic applications. However, experimental research on such low-temperature cavitation flow is difficult. Hence it is necessary to carry out numerical simulation research when studying the cavitation flow of working fluids in thermosensitive conditions.

Considering the complexity of flow conditions in hydraulic machinery, some researchers conduct research on the characteristics of cavitation flow in a C-D nozzle (Venturi), which is one of the typical cavitation flows [6-8]. And its different cavitation patterns, including supercavitation, cloud cavitation, and sheet cavitation are produced by changing the cavitation number σ or the pressure recovery number κ if the thermodynamic effects are neglected [9,10].

$$\sigma = \frac{p_{ref} - p_v}{0.5\rho V^2} \tag{1}$$

$$\kappa = \frac{p_1 - p_v}{p_1 - p_2} \tag{2}$$

While for other thermosensitive conditions, parameter of thermdynamic effets

$$\Sigma = \frac{\rho_v^2 L^2}{\rho_l^2 c_{pl} T_\infty \sqrt{\alpha_l}} \tag{3}$$

is defined by Brennen [11] to estimate the thermodynamic effects of cavitation, which depends only on the fluid temperature and the physical properties of the liquid.

Both experimental and numerical research of Venturi cavitation flow on thermosensitive conditions have lasted decades. In terms of the experimental research, Petkovšek et al. [12,13], Zhang et al. [14], and Ge et al. [15] conducted cavitation experiments on a Venturi with hot water. Watanabe et al. [16] analyzed the cavitation length and the cavitation instability in HFE liquid. Ohira et al. [17], Zhu et al. [18] Wei et al. [19], and Chen et al. [20,21] conducted experiments using LN_2. In the above study of typical cavitation flow considering thermodynamic effects, some experimental results are inconsistent with the theory that thermodynamic effects inhibit the development of cavitation, and there is a lack of comprehensive and systematic experimental research, resulting in the unclear influence of thermodynamic effects on the averaged and dynamic characteristics of the cavitation flow.

As for the numerical study, some research works didn't change the cavitation model and the thermodynamic effects of cavitation is considered by solving the energy equation and updating the physical properties of the fluid or calibrating the empirical coefficients [22,23]. The characteristic that the saturated vapor pressure of the working fluid is very sensitive to the temperature change is not considered enough in these cases. And some other research works further correct the saturated vapor pressure expression terms in the cavitation model and use B-factor [5,24] to estimate the temperature drop due to cavitation [25,26]. In such cases, the universality of B-factor still needs to be verified [22]. Last, some researchers corrected the evaporation and condensation source terms in the cavitation model [27,28]. The assumption in such kind of research is closer to the actual process of cavitation development. Among these studies, the correction method based on the ZGB cavitation model has better applicability and higher efficiency than others, which assumes that all the latent heat near the bubble wall is used for the evaporation process. However, due to the lack of systematic experiments, the existing studies mostly use the average characteristics of experiments obtained in the early stage [29] for simulation verification. Therefore, the simulation study of Veturi cavitation flow considering the thermodynamic effects need to be further carried out and compared with the experimental results to verify the effectiveness of the numerical simulation methods.

In short, some results of experimental research contradict each other. Numerical study on the effectiveness of the numerical simulation methods in the dynamic characteristics prediction of cavitation flow needs to be further investigated.

2. EXPERIMENTAL APPARATUS

It is found that when the cavitation number or thermodynamic parameter of the same liquid changes singly, the initial cavitation number when

the flow changes from non-cavitation to visible cavitation is different [30,31]. There is also no obvious change rule or trend. Even if the working fluid has been fully degassed before the experiment, the increase of cavitation nuclei in the liquid cannot be eliminated as experiments proceed. With the development of the experiment, the cavitation nuclei in the liquid increase, and the cavitation is more likely to occur, resulting in the gradual increase of the initial cavitation value. Considering that it is hard to control the influence of nuclei on cavitation flow in a circulating water tunnel, a blowdown-type cavitation tunnel is used in this experiment to reduce the influence of nuclei as much as possible through fully degassing pre-treatment. The blowdown-type cavitation tunnel uses the pressure difference between the two liquid storage tanks to drive the working fluids to flow through the experimental section, so the flow rate is gradually reduced in a single experiment.

The schematic diagram is shown in Fig. 1. The working fluid (degassed water in this paper) is stored in the upstream tank (150 *liters*). Driven by the differential pressure, it will flow along with the turbine flowmeter, honeycomb structure, contraction section, experimental section, expansion section, pneumatic valve, and finally to the downstream tank (30 *liters*). The upstream tank is designed larger to obtain a more stable upstream pressure and the downstream tank keeps open during the experiment, which makes each experiment last more than 30 seconds. Figure 2 shows the pressure change in the tanks during an example condition. As shown in the enlarged view, the pressure difference changed about 3% in 1 *s* and 0.6% in 0.1*s*. Also, the characteristic time scale in our experiments was <0.04 *s*. Therefore, cavitation events in 0.1 *s* were thought to be quasi-steady and we use the averaged values of p_{in}, p_{out}, and T during 0.1 *s* when calculating the κ and Σ. Two tanks are both connected to a vacuum pump and an air compressor to realize independent pressure regulation in the range of 0.03-0.8 *MPa*. Two 3 *kW* heating rods and a PT100 thermal resistance are installed in the upstream tank. Before experiments, the PID control system can be used to adjust and stabilize the temperature (290-360 *K*) of the water in the tank.

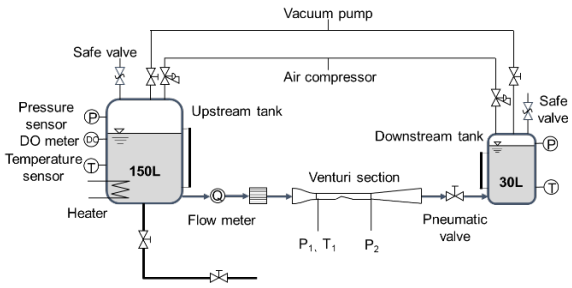

Figure 1. Schematic of the blowdown-type cavitation tunnel

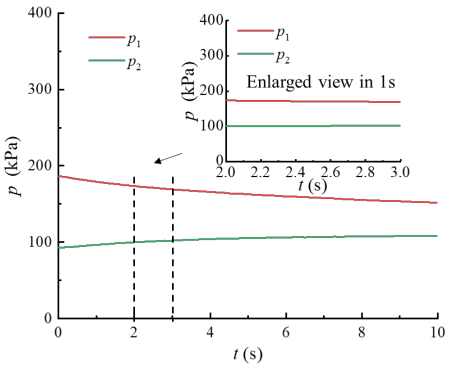

Figure 2. Pressure difference at p_{in}=230 *kpa*, p_{out}=100 *kpa*, and T=292 *K*

The honeycomb section, contraction, and expansion section are used to prevent flow separation and make the inflow of Venturi uniform. The experimental section is a contraction-diffusion Venturi made of plexiglass material. The specific size and structure are shown in Fig. 3. The inlet and outlet are 10×10 *mm* square sections and the throat height H_{th} is 5 *mm*. The constriction angle and divergent angle of the Venturi are 18 ^{o} and 8 ^{o} respectively. A variety of cavitation types can be generated by using this experimental apparatus.

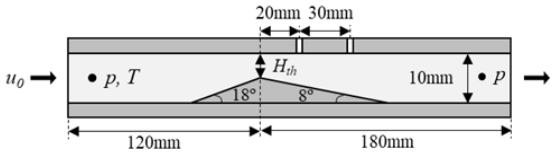

Figure 3. Detailed drawing of the convergent-divergent Venturi section

To capture the detailed characteristics of cavitation flow, the front and upper sides of the experimental section will be photographed by a high-speed camera (Phantom v2012). A specially designed mirror system shown in Fig. 4 enables the cameras to shoot both sides horizontally in front. Then, the high-speed photography of the upper side avoids the misjudgement of cavitation break-off caused by the superposition effect of spanwise cavitation. It is shooting at 10,000 *fps*, with a spatial resolution 1024 ×512 *pixels*, and an exposure time 2 μs.

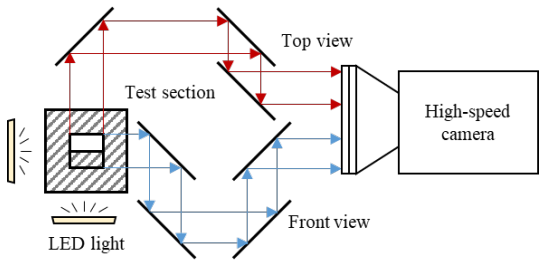

Figure 4. Schematic of the mirror system

The temperature of the incoming flow is measured with a Pt100 sensor with an uncertainty ±0.05 *K*. Pressure sensors are located in the two tanks, and before and after the Venturi section, with a measurement range of 0-1 *MPa* and uncertainty of ±0.025% *FS*. Two additional high-frequency dynamic pressure sensors are positioned respectively 20 *mm* and 50 *mm* downstream of the Venturi throat. They are all synchronous triggered.

3. NUMERICAL METHODS AND SETUP

3.1. Numerical setup

The computation domain is shown in Fig 5. The applied construction and dimensions of the Venturi in the simulations are consistent with that in the experiments. The height H_{in}=H_{out}=10 *mm*, and H_{th}=5 *mm*. Angles of the C-D square nozzle are α_1=18º and α_2=8º respectively. The distance between the inlet and the Venturi throat is $10H_{in}$, which is consistent with the position of the pressure and temperature measuring points at the experimental inlet, and the outlet is appropriately extended, which is $35H_{in}$ from the Venturi throat.

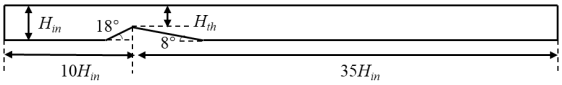

Figure 5. Computation domain

Because the experimental results mainly show the two-dimensional characteristics, it is set as a two-dimensional model with only one layer of the grid in the spanwise direction (the spanwise width is 1mm). water in specific temperature was used as the working fluid at the inlet. Its uniform velocity at the inlet of the upstream channel and constant pressure at the outlet of the downstream channel were chosen as the boundary conditions. To control the κ, the inlet velocity is adjusted to obtain the specific p_{in}. The sidewall of the computation domain is set as the symmetrical boundary condition. And "No-slip" conditions were imposed on all the other stationary walls.

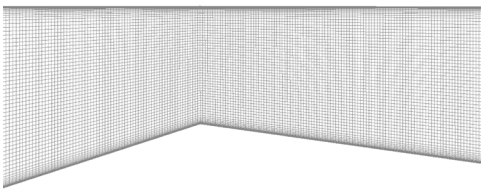

Figure 6. Mesh of C-D square nozzle and its refinement

Structured grid systems were developed by using commercial software ICEM-CFD in this study. The simulations were conducted in ANSYS CFX. Wall function varied with the turbulence model. Schlable wall function is used when the turbulence model is *k-ε,* and RNG *k-ε.* Enhanced wall treatment is used for SST *k-ω.* Because Schlable wall function adds limit to force Standard wall functions to use logarithmic law when y^+ are too small and the same grid is used for all the models. The first boundary grid layer is set located in a viscous sublayer, required by SST *k-ω*. Therefore, local grid refinements to the boundary layers were applied at the walls and the thickness of the first grid is specified as 6×10^{-5} *mm* with a size growth ratio of 1.2. The maximum y^+ on the diverging wall is about 2 in steady simulations. The grid around the Venturi contraction and diffusion is shown in Fig. 6.

In order to resolve the real transient evolution of cavitating flow, the time step needs to be set as 1.25×10^{-6} *s* (which is equivalent to $H_{th}/200U_{th}$). However, to save the computational resources, it is set as 5×10^{-6} *s* when we found the results changed little. The Courant number $C = u\Delta t/\Delta s < 1$ (where u, Δt, and Δs are the characteristic flow velocity, the time step size, and typical cell size, respectively). Second order backorder Euler upwind is chosen as transient scheme. The transient simulation was started from a steady case. Simulation convergence was achieved when the residual error was lower than 10^{-6}, or the variation of the operational parameter inlet pressure p_{in} was below 0.01%.

3.2 Governing equations

Numerical simulations of cavitating flow in this paper are established based on the three-dimensional compressible Navier–Stokes equations. The homogeneous mixture model is chosen. The conservation equations of mass, momentum, and energy are as follows [32]:

Continuity equation

$$\frac{\partial \rho_m}{\partial t}+\frac{\partial\left(\rho_m u_j\right)}{\partial x_j}=0 \tag{4}$$

Momentum equation

$$\frac{\partial}{\partial t}\left(\rho_m u_i\right)+\frac{\partial\left(\rho_m u_i u_j\right)}{\partial x_j}$$

$$=-\frac{\partial p}{\partial x_i}+\nabla \tau_{ij}+S \tag{5}$$

$$\tau_{ij}=\mu_{eff}\left[\left(\frac{\partial u_i}{\partial x_j}+\frac{\partial u_j}{\partial x_i}\right)-\frac{2}{3}\delta_{ij}\frac{\partial u_k}{\partial x_k}\right]$$

Energy equation

$$\frac{\partial\left(\rho_m c_p T\right)}{\partial t}+\frac{\partial}{\partial x_j}\left(\rho_m u_j c_p T\right) \tag{6}$$

$$=\nabla\cdot\left(k_{eff}\nabla T\right)+S_E$$

$S, \mu_{eff}, k_{eff}, S_E$ represent respectively, the source item generated by volume force or user-defined,

effective viscosity, the effective thermal conductivity, the volumetric heat sources, and the volume fraction of the vapor phase.

3.4. Cavitation model

The cavitation model is important in cavitation numerical simulation. At present, the widely used transport equation model is based on the homogeneous mixture model. The mass conversion between two phases is characterized by the evaporation source term $\dot{m}^+$ and the condensation source term $\dot{m}^-$. The volume fraction or mass fraction of two phases in the flow process is obtained by solving the transport equation. The expressions of two typical transport equations are as follows:

$$\begin{aligned} &\frac{\partial\left(\rho_l\alpha_l\right)}{\partial t}+\nabla\cdot\left(\rho_l\alpha_l\vec{u}\right)=\dot{m}^+ +\dot{m}^- \\ &\frac{\partial\rho_m f_v}{\partial t}+\nabla\cdot\left(\rho_m f_v\vec{u}\right)=\dot{m}^+ +\dot{m}^- \end{aligned} \tag{7}$$

Zwart-Gerber-Belamri (ZGB) cavitation model derived from the Rayleigh-Plesset equation [33] is mainly used in numerical simulations. In the derivation process, the temperature change is not considered, and the influence of surface tension and viscosity are both ignored. The expression of transport source term is as follows:

$$\begin{aligned} &p\le p_v\left(T_\infty\right) \\ &\qquad \dot{m}^- = C_{vap}\frac{3\alpha_{nuc}\rho_v\left(1-\alpha_v\right)}{R_B}\sqrt{\frac{2\left(p_v\left(T_\infty\right)-p\right)}{3\rho_l}} \\ &p> p_v\left(T_\infty\right) \\ &\qquad \dot{m}^+ = C_{\mathrm{cond}}\frac{3\alpha_v\rho_v}{R_B}\sqrt{\frac{2}{3}\frac{\left(p-p_v\left(T_\infty\right)\right)}{\rho_l}}, \end{aligned} \tag{8}$$

where α_{nuc} and R_B are the volume fraction of non-condensable gas and the mean radius of bubble separately. C_{vap} and C_{cond} are empirical constant.

Take thermodynamic effects into consideration, a modified model is also applied [28,34,35]:

$$\begin{aligned} &p\le p_v(T) \qquad \dot{m}^- = C_{vap}\frac{3\alpha_{nuc}\rho_v\left(1-\alpha_v\right)}{R_B} \\ &\left(\sqrt{\frac{2}{3}\frac{\left(P_v(T)+P_{\mathrm{turb}}-P\right)}{\rho_l}}-\frac{\rho_l C_{pl}\sqrt{\lambda_l}\left(T_\infty-T\right)}{\rho_v L\sqrt{t}}\right) \\ &p> p_v(T) \qquad \dot{m}^+ = C_{\mathrm{cond}}\frac{3\alpha_v\rho_v}{R_B} \\ &\left(\sqrt{\frac{2}{3}\frac{\left(P_v(T)+P_{\mathrm{turb}}-P\right)}{\rho_l}}-\frac{\rho_l C_{pl}\sqrt{\lambda_l}\left(T_\infty-T\right)}{\rho_v L\sqrt{t}}\right) \end{aligned} \tag{9}$$

3.3. Turbulence model

Several turbulence models are chosen to compare in this paper, such as SST *k-ω*, *k-ε*, and RNG *k-ε*, which are the extensive application of the Reynolds-averaged Navier–Stokes-based models in simulating the cavitating flow.

4. RESULTS AND DISCUSSION

4.1. Image post-processing

There develops an attached cavity cloud at the throat of the Venturi. The mean area or length of such a cavity cloud and its oscillation are important parameters for quantitative analysis. For cloud cavitation, the cavity cloud grows larger and longer at first, then a large part of the cloud breaks off at the position near the throat, and finally, the remaining part grows again. The length and its oscillation frequency can be obtained from image post-processing of high-speed video.

The same image post-processing method in Reference [14] is conducted in the present research to estimate the mean length of attached cavitation $\overline{L}_{cav}$,the mean cavitation area $\overline{A}_{cav}$ and frequency *f*. The first step is choosing a background image that is a non-cavitating condition and using it to normalize the instantaneous image intensity distribution *I* of each frame. Thus calculate the 'grey-level' of $(I\text{-}I_0)/I_0$ for each pixel. All the frames of the video which contain several cavity cloud circles are processed as above, then mean values and standard deviations are determined. Suppose that black (grey-level=0) is totally liquid and white is contrast, $\overline{A}_{cav}$ is integrated. The position of the cavity cloud closure is then located where the standard deviation of the grey level reaches its maximum value. Assume that the mean values and the standard deviations did not change significantly when more than 5000 images were analyzed [7]. The mean cavitation length $\overline{L}_{cav}$ is measured from the Venturi throat to the closure line with an uncertainty of <2%. Frequency *f* is got from the FFT results of the average value of the 10×10 *pixels* region shown in Fig. 7(b).

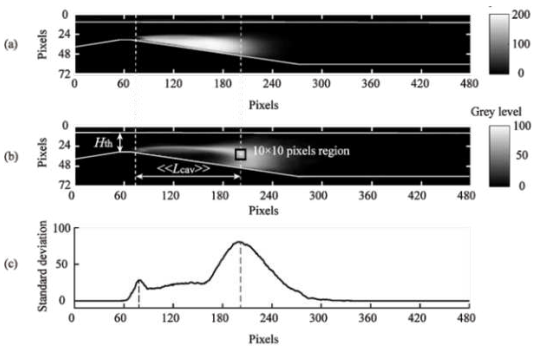

Figure 7. Image post-processing [cited from Reference 14]

4.2. Numerical validation with experiments

The averaged cavitation area of simulation results is calculated by the equation:

$$\overline{A}_{cav}=\frac{1}{W\Delta t}\sum_{t=0}^{\Delta}\left(\sum_{i,j}\alpha_{i,j}(t)V_{i,j}(t)\right), \tag{10}$$

where $a_{i,j}$ and $V_{i,j}$ represent the volume fraction and volume of a grid cell, respectively. W and Δt represent the spanwise width of the computational model and the time length for time averaging, respectively.

As preliminary tests, steady simulations using five mesh systems were carried out to find out the plausible number of grids. Uniform velocity at the inlet u_{th} is 20.02 *m/s* and constant pressure at the outlet of the downstream channel p_{out} is 100 *kPa* here. The results are shown in Fig. 8: $\overline{A}_{cav}$ becomes almost constant when the number of grids is greater than 2.29×10^5. Therefore, the mesh system with a 3.75×10^5 grid is chosen for the following simulation.

Table 1 shows the comparison of averaged cavitation area $\overline{A}_{cav}$ and frequency f between the transient-flow simulations and experimental results. Simulation results with different turbulence models are also compared. It shows that simulation results with SST k-ω model and k-ε model have less than 2% error in $\overline{A}_{cav}$ and k-ε model has only 1.15% error in f with the results of the experiments. It shows that the structure of Venturi cavitation flow is better predicted by the present simulation with the k-ε model. Therefore, it is chosen for further simulations.

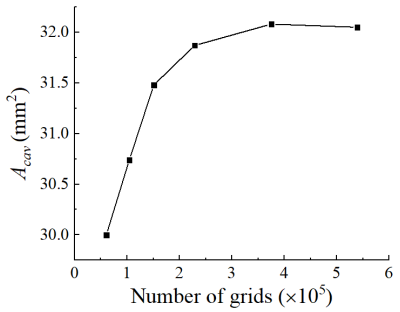

Figure 8. Grid independence test at u_{th}=20.02 *m/s*, p_{out}=100 *kPa*, T=292 *K* (steady simulation)

Table 1. Comparison between simulations and experiments at u_{th}=20.02 *m/s*, p_{out}=100 *kPa*, T=292 *K* (transient simulation)

	$\overline{A}_{cav}$: Experiment	$\overline{A}_{cav}$: Simulation		Error (%)
$\overline{A}_{cav}$ (mm^2)	30.38	SST k-ω	30.87	1.61
		k-ε	30.74	1.18
		RNG k-ε	28.93	4.77
f (Hz)	303.3	SST k-ω	294.0	3.07
		k-ε	299.8	1.15
		RNG k-ε	318.9	5.14

4.3. The cavitating Venturi flow

Set the pressure of the upstream tank to 300 *kPa*, and the downstream tank is open. As mentioned before, cavitation will occur at the throat of the venturi and develop downstream after opening the valve. In one blowdown experiment, with the decrease of the pressure difference, the velocity at the throat decreases, and the type of cavitation undergoes a transition from supercavitation (Fig. 9(a)), to cloud cavitation (Fig. 10), and finally to sheet cavitation (Fig. 9(b)). Supercavitation occurs at the beginning, with the largest flow velocity at the throat and the smallest κ. On this condition, the cavitation is fully developed, and the cavitation area exceeds the visualization window. At last of the experiment, it becomes to sheet cavitation. Under this condition, the length of the attached cavity cloud changes very little, and its shape is relatively stable.

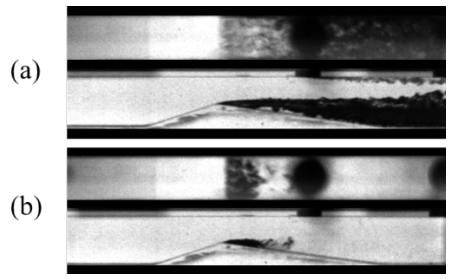

Figure 9. (a) super cavitation κ=1.31;(b) sheet cavitation κ=5.40 (T=292 *K*, Σ=3.43)

As for cloud cavitation, there exists a periodic shedding phenomenon. As shown in Fig. 10, the cavitation can be regarded as two parts of attached cavity cloud and detached cavity clouds/clusters. The length of the attached cavity cloud increases continuously until the fracture occurs near the throat, and then detached cavity clouds/clusters will fall off downstream. Subsequently, the attached cavity cloud regenerates, and its length will grow further as the cavitation develops. While the detached cavity clouds/clusters continue to move downstream and finally collapse.

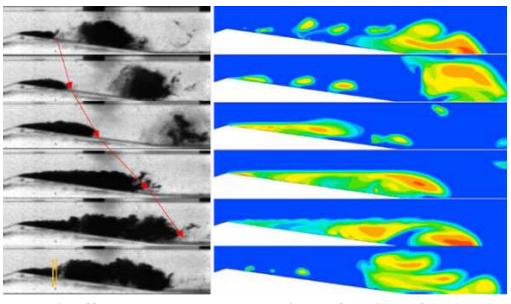

Figure 10. Evolution of cloud cavitation at T=292 *K*, Σ=3.43, κ=1.85 (results of experiment and transient-flow simulation)

4.4. Influence on mean characteristic

According to the definition of Σ, which is used to characterize the degree of the cavitation thermodynamic effects, it is only related to the temperature/physical properties of the working

liquid. Therefore, when experiment conducted at the same temperature, Σ keeps almost the same, while kappa number κ changes. Results in Fig. 11 show the mean area of cavitation (simulation results) and mean length (experimental results) decreases with the increase of κ. Results in Fig. 12 show that they also decrease with the increase of Σ or temperature. At a larger Σ, the cavitation is more stable and the collapse and rebound processes of cavity clouds and clusters at the Venturi throat are less violent in our experiments.

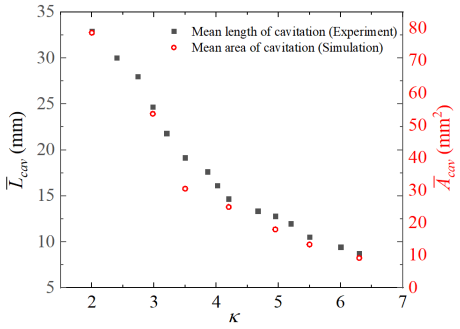

Figure 11. $\overline{L}_{cav}$ of experimental and $\overline{A}_{cav}$ against kappa number κ (T=292 K, Σ=3.43)

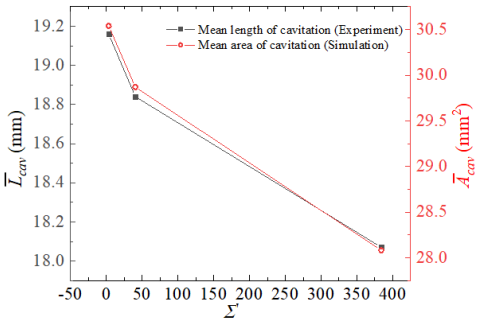

Figure 12. $\overline{L}_{cav}$ and $\overline{A}_{cav}$ against parameter of thermodynamic effect Σ (κ=3.49)

5. CONCLUSIONS

Experimental and numerical research of a specific Venturi structure on the water in a range of 290-360 K are both conducted. A corrected ZGB cavitation method is used and different turbulence models are compared. k-ε model mostly suits such kind of cavitation flow. Both averaged and dynamic results of experimental measurement and numerical results agree well, which means this numerical method can be used in simulations to fill more thermosensitive conditions and obtain more information about flow in the future.

Some conclusions are summarized: 1. Results show that the mean cavitation length of experiments $\overline{L}_{cav}$ and the mean cavitation area of simulations $\overline{A}_{cav}$ have the same trend; 2. $\overline{L}_{cav}$ and $\overline{A}_{cav}$ both decrease as κ increases; 3. They also decrease as Σ increases, which means the thermodynamic effects suppress the cavitation flow and the cavitation-related pressure recovery is reduced.

ACKNOWLEDGEMENTS

This work was partially supported by the National Nature Science Foundation of China (No.52076120 and No.52079066).

REFERENCES

[1] Luo, X. W., Ji, B., & Tsujimoto, Y. (2016). A review of cavitation in hydraulic machinery. Journal of Hydrodynamics, 28(3), 335-358.

[2] Lu, G., Zuo, Z., Sun, Y., Liu, D., Tsujimoto, Y., & Liu, S. (2017). Experimental evidence of cavitation influences on the positive slope on the pump performance curve of a low specific speed model pump-turbine. Renewable Energy, 113, 1539-1550.

[3] Brennen, C. E., Hydrodynamics of pumps; Cambridge University Press, New York, 2011; pp. 114.

[4] Franc, J.P.; Michel, J.M., Fundamentals of cavitation; Springer science & Business media, Berlin, 2006; pp. 10.

[5] Stahl H. A.; Thermodynamic aspects of cavitation in centrifugal pumps, Trans. Am. Soc.Mech. Eng 1956, 78, 1691.

[6] Tomov, P., Khelladi, S., Ravelet, F., Sarraf, C., Bakir, F., & Vertenoeuil, P. (2016). Experimental study of aerated cavitation in a horizontal Venturi nozzle. Experimental Thermal and Fluid Science, 70, 85-95.

[7] Danlos, A., Ravelet, F., Coutier-Delgosha, O., & Bakir, F. Cavitation regime detection through proper orthogonal decomposition: dynamics analysis of the sheet cavity on a grooved convergent–divergent nozzle. International Journal of Heat and Fluid Flow, 2014. 47, 9-20.

[8] Jahangir, S., Hogendoorn, W., & Poelma, C. (2018). Dynamics of partial cavitation in an axisymmetric converging-diverging nozzle. International Journal of Multiphase Flow, 106, 34-45.

[9] Coutier-Delgosha, O., Devillers, J. F., Pichon, T., Vabre, A., Woo, R., & Legoupil, S. (2006). Internal structure and dynamics of sheet cavitation. Physics of fluids, 18(1), 017103.

[10]Callenaere, M., Franc, J. P., Michel, J. M., & Riondet, M. (2001). The cavitation instability induced by the development of a re-entrant jet. Journal of Fluid Mechanics, 444, 223-256.

[11]Brennen, C. (1973). The dynamic behavior and compliance of a stream of cavitating bubbles. Journal of Fluids Engineering, 95(4), 533-541.

[12]Petkovšek M, Dular M. IR measurements of the thermodynamic effects in cavitating flow[J]. International Journal of Heat and Fluid Flow, 2013, 44: 756-763.

[13]Petkovšek M, Dular M. Observing the thermodynamic effects in cavitating flow by IR thermography [J]. Experimental Thermal and Fluid Science, 2017, 88: 450-460.

[14]Zhang H, Zuo Z, Mørch K A, et al. 2019. Thermodynamic effects on Venturi cavitation characteristics. Physics of Fluids [J], 31: 097107.

[15]Ge M, Petkovšek M, Zhang G, et al. Cavitation dynamics and thermodynamic effects at elevated temperatures in a small Venturi channel[J]. International Journal of Heat and Mass Transfer, 2021, 170: 120970.

[16] Watanabe S, Enomoto K, Yamamoto Y, et al. Thermal and dissolved gas effects on cavitation in a 2-D convergent-divergent nozzle flow [C]// Proceedings of the ASME 2014 4th Joint US-European Fluids Engineering Division Summer Meeting Collocated with the ASME 2014 12th International Conference on Nanochannels, Microchannels, and Minichannels, 2014.

[17]Ohira K, Nakayama T, Nagai T 2012. Cavitation flow instability of subcooled liquid nitrogen in converging–diverging nozzles. Cryogenics [J], 52: 35-44.

[18]Zhu J, Xie H, Feng K, et al. 2017. Unsteady cavitation characteristics of liquid nitrogen flows through Venturi tube. International Journal of Heat and Mass Transfer [J], 112: 544-552.

[19]Wei A, Yu L, Gao R, et al. Unsteady cloud cavitation mechanisms of liquid nitrogen in convergent–divergent nozzle[J]. Physics of Fluids, 2021, 33(9): 092116.

[20]Chen T, Chen H, Liang W, et al. Experimental investigation of liquid nitrogen cavitating flows in converging-diverging nozzle with special emphasis on thermal transition[J]. International Journal of Heat and Mass Transfer, 2019, 132: 618-630.

[21]Chen T, Chen H, Liu W, et al. 2019. Unsteady characteristics of liquid nitrogen cavitating flows in different thermal cavitation mode. Applied Thermal Engineering [J], 156: 63-76.

[22]Hosangadi A, Ahuja V. Numerical study of cavitation in cryogenic fluids[J]. Journal of Fluids Engineering, 2005, 127(2): 267-281.

[23]Long X, Liu Q, Ji B, et al. Numerical investigation of two typical cavitation shedding dynamics flow in liquid hydrogen with thermodynamic effects[J]. International Journal of Heat and Mass Transfer, 2017, 109: 879-893.

[24]Stepanoff A J. Cavitation Properties of Liquids[J]. ASME Journal of Engineering for Power, 1964, 86: 195.

[25]Tani N, Tsuda S, Yamanishi N, et al. Development and validation of new cryogenic cavitation model for rocket turbopump inducer[C]//Proceedings of the 7th International Symposium on Cavitation(CAV2009), Michigan, USA, 2009.

[26]Chen T, Wang G, Huang B, et al. Numerical study of thermodynamic effects on liquid nitrogen cavitating flows[J]. Cryogenics, 2015, 70: 21-27.

[27]Zhang Yao, Luo Xianwu, et al. A thermodynamic cavitation model for cavitating flow simulation in a wide range of water temperatures [J]. Chinese Physics Letters, 2010, 27(1):016401.

[28]Sun T, Zong Z, Zou L, et al. Numerical investigation of unsteady sheet/cloud cavitation over a hydrofoil in thermo-sensitive fluid[J]. Journal of Hydrodynamics, Ser. B, 2017, 29(6): 987-999.

[29]Hord J. Cavitation in liquid cryogens. 2: Hydrofoil[R]. National Aeronautics and Space Administration, Lewis Research Center, 1973.

[30]Zhu J, Wang S, Zhang X. Influences of thermal effects on cavitation dynamics in liquid nitrogen through Venturi tube[J]. Physics of Fluids, 2020, 32(1): 012105.

[31]Kikuta K, Yoshida Y, Hashimoto T, et al. Influence of rotational speed on thermodynamic effect in a cavitating inducer [C]// Proceedings of the ASME 2009 Fluids Engineering Division Summer Meeting, 2009.

[32]Christopher Earls Bernnen. Fundamentals of multiphase flow. California Institute of Technology, 2003:19~51.

[33]Zwart P J, Gerber A G, Belamri T. A two-phase flow model for predicting cavitation dynamics [C].// In Fifth International Conference on Multiphase Flow,Yokohama, Japan, 2004.

[34] Zhang S, Li X, Zhu Z. Numerical simulation of cryogenic cavitating flow by an extended transport-based cavitation model with thermal effects[J]. Cryogenics, 2018: 89-104.

[35]Li X J, Shen T J, Li P C, et al. Extended compressible thermal cavitation model for the numerical simulation of cryogenic cavitating flow[J]. International Journal of Hydrogen Energy, 2020, 45:10104-10118.